ORAL DISEASES
Leading in Oral, Maxillofacial, Head & Neck Medicine

Development of lung metastases in mouse models of tongue squamous cell carcinoma

Journal:	*Oral Diseases*
Manuscript ID	ODI-06-20-OM-8465.R1
Manuscript Type:	Original Manuscript
Date Submitted by the Author:	14-Jul-2020
Complete List of Authors:	Marcazzan , Sabrina; Università degli Studi di Milano, Dipartimento di Scienze Biomediche, Chirurgiche e Odontoiatriche; Houston Methodist Research Institute, Department of Nanomedicine Dadbin, Ali; Houston Methodist Research Institute, Department of Nanomedicine Brachi, Giulia; Politecnico di Torino, Department of Mechanical and Aerospace Engineering; Houston Methodist Research Institute, Department of Nanomedicine Blanco, Elvin; Houston Methodist Research Institute, Department of Nanomedicine Varoni, Elena Maria; Università di Milano, Scienze Biomediche, Chirurgiche ed Odontoiatriche Lodi, Giovanni; Università degli Studi di Milano, Dipartimento di Scienze Biomediche, Chirurgiche e Odontoiatirche Ferrari, Mauro; Houston Methodist Research Institute, Department of Nanomedicine
Keywords:	Oncology, cancer and pre-cancer < Oncology, histopathology < Pathogenesis

Development of lung metastases in mouse models of tongue squamous cell carcinoma

Running title: Mouse models of metastatic tongue cancer

Keywords: head and neck cancer, oral cancer, animal models, distant metastases, lymph node metastases

Sabrina Marcazzan[1,2], Ali Dadbin[2], Giulia Brachi[2,3], Elvin Blanco[2], Elena Maria Varoni[1], Giovanni Lodi[1,*] and Mauro Ferrari[2,*]

[1]Dipartimento di Scienze Biomediche, Chirurgiche e Odontoiatriche, Università degli Studi di Milano, Beldiletto Street 1/3, Milan 20142, Italy. Electronic addresses: sabrina.marcazzan@tum.de; elena.varoni@unimi.it; giovanni.lodi@unimi.it

[2]Department of Nanomedicine, Houston Methodist Research Institute, 6670 Bertner Avenue, Houston, TX 77030, USA. Electronic addresses: eblanco@houstonmethodist.org; mferrari@arrowheadpharma.com; ddadbin@hotmail.com

[3]Department of Mechanical and Aerospace Engineering, Politecnico di Torino, Duca degli Abruzzi Street 24, Turin 10129, Italy. Electronic address: giulia.brachi@polito.it

* co-shared authorship

Corresponding Author:

Dr. Sabrina Marcazzan

Institute of Biological and Medical Imaging (IBMI),

Helmholtz Zentrum München (HMGU)

Ingolstädter Landstr.1 85764 Neuherberg, Germany

Tel: +49 89 4140 6795

Fax: +49 89 4140 6796

Email: sabrina.marcazzan@tum.de

Co-corresponding Author:
Prof. Giovanni Lodi
Dipartimento di Scienze Biomediche, Chirurgiche e Odontoiatriche
Università degli Studi di Milano
Beldiletto Street 1/3, Milan, 20142, Italy
Tel. + 39 02 50319021
Fax. + 39 02 50319041
Email: giovanni.lodi@unimi.it

Date of submission: 06/06/2020

Abstract

Objective

Oral Squamous Cell Carcinoma (OSCC) represents 3-4% of all cancers. Despite the increasing incidence of OSCC distant metastasis and poor prognosis, few animal models of OSCC distant metastasis have been reported. In this study, we established mouse models of OSCC lung metastasis by orthotopic and tail vein injection of new OSCC cell lines.

Methods

For the tail vein model, we used a novel cell line isolated from lung metastases reproduced in vivo after intravenous injection of HSC-3 GFP/luciferase cells and sorted for GFP expression (HSC-3 M1 GFP/luciferase). Lung metastases were assessed by imaging techniques and further confirmed by histology. For the orthotopic model, HSC-3 GFP/luciferase cells were injected into the tongue of athymic nude mice. The primary tumor and metastases were assessed by in vivo imaging, histology, and immunohistochemistry.

Results

The orthotopic model presented spontaneous lung metastases in 50% of the animals and lymph node metastases were present in 83% of cases. In the tail vein model, a lung metastasis rate of 60% was observed.

Conclusions

Lung metastases were successfully reproduced by orthotopic and tail vein injection. Since lymph node metastases were present, the orthotopic model with HSC-3 GFP/luciferase cells may be suitable to investigate metastatic dissemination in OSCC.

1.Introduction

Oral Squamous Cell Carcinoma (OSCC) is classified among Head and Neck Squamous Cell Carcinomas (HNSCC), the sixth most common cancer worldwide, and represents 3-4% of all human cancers (Chi, Day, & Neville, 2015; Furness et al., 2011). Poor prognosis and a 5-year survival rate of less than 50% characterise advanced stages of OSCC (de Visscher et al., 2013; Steeg, 2016; Sutton, Brown, Rogers, Vaughan, & Woolgar, 2003). The combination of surgery, radiation, and chemotherapy has not reduced the incidence of distant metastases (DMs), which increased up to 10% between 2005 and 2015 (Bernier et al., 2004; Furness et al., 2011; Steeg, 2016). In patients affected by OSCC DMs, the lungs are the most frequent site reported (81.5%) followed by the bone (46.3%), mediastinum (18.5%), and liver (16.6%) (Irani, 2016a; Naruse et al., 2016; Osaki et al., 2000; Takahashi et al., 2014). Few therapeutic options are currently available for those patients (Naruse et al., 2016; Noguti et al., n.d.; Sutton et al., 2003) and improvements in the quality of life and overall survival have been reported only recently with nivolumab (Harrington et al., 2017).

Few animal models of OSCC metastasis have been described (Bais, Kukuruzinska, & Trackman, 2015; Mognetti, Di Carlo, & Berta, 2006). Indeed, the frequently used chemically induced OSCC animal models require a long time for tumor growth and present a low metastasis rate (Q. Li et al., 2020; Mognetti et al., 2006). Additionally, subcutaneous animal models are inadequate to mimic the metastatic growth of human OSCC due to differences in the tumor microenvironment (Bais et al., 2015; Mognetti et al., 2006; Sano & Myers, 2009). Indeed, Myers et al. (Myers, Holsinger, Jasser, Bekele, & Fidler, 2002) reported that OSCC cells injected in the orthotopic site were more tumorigenic than those injected subcutaneously. The development of OSCC lung metastasis by intravenous (IV) injection of tumor cells has been reported in only a few studies (Chen, Liu, et al., 2019; Hier, Black, Shenouda, Sadeghi, & Karp, 1995; Hyakusoku et al., 2016; Mognetti et al., 2006). However, this approach has limitations such as the lack of a primary tumor and regional lymph node metastases (Hyakusoku et al., 2016; Mognetti et al., 2006; Saxena & Christofori, 2013). Genetically engineered mouse models of OSCC have also been developed but their low metastasis rate and the presence of multiple primary tumors (e.g. in the skin and oral cavity) in a single animal limit their use for studying metastatic dissemination (Ishida et al., 2017; Q. Li et al., 2020; Mognetti et al., 2006).

Moreover, most mouse models of OSCC metastasis reported in the literature are obtained by orthotopic implantation of human and/or murine cell lines (Ishida et al., 2017; Q. Li et al., 2020). Such models are superior because they closely resemble the metastatic growth of human OSCC (Bais et al., 2015; Ishida et al., 2017; Mognetti et al., 2006; Sano & Myers, 2009). Indeed, orthotopic models exhibit a high

prevalence of regional lymph node metastases, which allowed researchers to discover the important role played by VEGF in lymphangiogenesis (S Kawashiri et al., 1999; Shuichi Kawashiri et al., 2009; Mognetti et al., 2006; Noguchi, Kawashiri, Tanaka, Kato, & Nakaya, 2003; Sugiura et al., 2009). However, only a few orthotopic models present DMs (especially lung metastasis) (Hasegawa et al., 2017; Shuichi Kawashiri et al., 2009; Q. Li et al., 2020; Lou, Kellman, Hutchison, & Shillitoe, 2003; Masood et al., 2013; Mognetti et al., 2006; Patel et al., 2011). Since the mechanism of OSCC DM dissemination is still poorly understood, preclinical animal models of OSCC lung metastasis are needed to evaluate the development of DMs.

Over twenty years ago, Matsui and co-workers (Matsui, Ota, Ueda, Tanino, & Odashima, 1998) developed a primary OSCC model by orthotopically injecting a high dose of HSC-3 cells into nude mice. They reported a low (10%) frequency of DMs. The purpose of this study was to develop an orthotopic model for the study of OSCC metastasis using HSC-3 cells genetically modified to allow in vivo bioluminescent imaging. In addition, we established another mouse model of OSCC lung metastasis by IV injection of the novel cell line HSC-3 M1 GFP/luciferase derived from HSC-3 lung metastases.

2.Materials and Methods

2.1 Cell line and cell morphology

HSC-3 cells from human tongue SCC were purchased from the Japanese Collection of Research Bioresources (JCRB) Cell Bank (n°JCRB0623). Cells were cultured in DMEM containing 10% fetal bovine serum (FBS) and 1% penicillin-streptomycin (PS). They were maintained at 37°C in a humidified atmosphere of 5% CO_2 and 95% air. To assess cell morphology, HSC-3 cells were plated in a 4-well chamber slide ($2x10^4$ cells/chamber). After 24 hours, the cells were washed three times with PBS, fixed with 4% paraformaldehyde in PBS and then stained with Alexa Fluor 488 phalloidin (1:200; Invitrogen™, Waltham, Massachusetts, USA) and DAPI (4 µg/ml) for 20 and 3 minutes respectively. Slides were then mounted using ProLong Gold Antifade Mountant (Invitrogen™, Waltham, MA, USA). Z-stack images (1.10 µm step) were acquired with FluoViewTM FV1000 Confocal Microscope (Olympus, Tokyo, Japan) and processed using ImageJ/Fiji software (Schindelin et al., 2012).

2.2 Cell transduction, sorting, and In Vivo Imaging System (IVIS)

In order to generate a stable HSC-3 cell line expressing GFP and luciferase (HSC-3 GFP/Luc), HSC-3 cells were transduced with a lentivirus packed with a plasmid carrying both GFP and luciferase genes (Xu et al., 2016). The lentivirus was generously provided by Dr. Junhua Mai, Department of Nanomedicine, Houston Methodist Research Institute. For the lentiviral infection, HSC-3 cells were plated in a 6-well plate and incubated overnight with lentivirus and DMEM media (1:2). Transduced HSC-3 GFP/Luc cells were then selected by Fluorescence Activated Cell Sorting (FACS) for GFP expression using a BD FACSAria II Cell Sorter (BD Biosciences, San Jose, CA, USA). Sorted HSC-3 GFP/Luc cells were cultured as indicated above. To measure the luciferase expression, sorted HSC-3 GFP/Luc cells were serially diluted in DMEM in a 96-well plate and 50 µL of D-luciferin (15 mg/ml) was added to each well 10 minutes before imaging. Luciferase expression was evaluated by IVIS Spectrum In Vivo Imaging System and then quantified following the manufacturer's instructions (PerkinElmer Inc., Waltham, MA, USA).

2.3 Isolation of HSC-3 M1 cell line

All animal experiments were performed following a protocol approved by the Institutional Animal Care and Use Committee (IACUC) at the Houston Methodist Research Institute (date of approval: 31/7/2017; ID:IS00004187) and in accordance with the National Institutes of Health Guide for the Care and Use of Laboratory Animals. The experimental animals were housed in individually ventilated cages with controlled airflow in light-controlled rooms (12 hours of light). Male (n=5) athymic nude-Foxn1^{nu} mice (Envigo, Indianapolis, IN, USA), 5-6 weeks old, weight 24.84 ± 2.15 g were injected with $1x10^5$ HSC-3

GFP/Luc cells in 100 µl of PBS into the tail vein. One mouse which presented lung metastases was sacrificed 34 days after injection and the lungs were collected. After the digestion of the minced lungs with collagenase IV (0.7 mg\ml in D-PBS), the cell suspension was cultured as described above.

2.4 Cell sorting and IVIS of HSC-3 M1 cell line

After two passages, HSC-3 M1 GFP/Luc cells were selected from the cells isolated from the lungs by FACS for GFP expression. Pure sorted cells were then grown in DMEM containing 10% FBS and 1% PS. The luciferase expression and the cellular morphology were then evaluated following the same procedure used for the HSC-3 GFP/Luc cell line.

2.5 Orthotopic model of OSCC lung metastasis

For the orthotopic model, 5-6 week-old male (n=5) and female (n=10) athymic nude-Foxn1^{nu} mice (Envigo, Indianapolis, IN, USA), were used (male weight 25.30 ± 2.20 g; female weight 21.35 ± 1.03 g). Before the procedure, analgesia with buprenorphine SR was provided to the animals (1 mg/kg SC). HSC-3 GFP/Luc cells (50,000) suspended in 20 µl of PBS were then injected into the left side of the tongue submucosa using an insulin syringe with a 28G 1/2 needle after anaesthetizing the animals with 3% isoflurane. After the procedure, the mice were fed with a soft food diet to reduce discomfort, monitored closely and weighed periodically. When human endpoints were reached (20% of weight loss, dehydration, inappetence), the animals were sacrificed through an anaesthetic overdose followed by cervical dislocation. The remaining athymic nude mice were sacrificed with the same procedure 11 (male) or 8 (female) weeks after cell transplantation.

2.6 Non-orthotopic model of OSCC lung metastasis

For the IV model, the new HSC-3 M1 GFP/Luc cell line was used. Female athymic nude-Foxn1^{nu} mice (7-8 weeks old, n=5, Envigo, Indianapolis, IN, USA), with an average weight of 21.22 ± 0.70 g, were injected with 0.5x10^{6} cells suspended in 100 µl of PBS into the tail vein. Mice were sacrificed as reported above when the human endpoints were reached or 6 weeks after the injection.

2.7 In vivo and ex vivo IVIS and signal quantification

Primary tumor and/or lung metastasis growth was monitored periodically by bioluminescence imaging in anaesthetised mice (isoflurane 2-3%), which were intraperitoneally (IP) injected with 200 µl of luciferin in PBS (15 mg/kg) 15 minutes prior to imaging. Ex vivo imaging of mouse organs was performed as follows: luciferin was administered IP to each mouse before sacrifice. Organs and tissues of interests were then collected and imaged to detect the presence of the primary tumor and/or metastasis. Finally,

the bioluminescence intensity was quantified by defining the bioluminescence region of interest (ROI) for tongue tumors and metastasis. Data were reported as photons/s as per the instructions (Aura software, Spectral Instruments Imaging, LLC, USA).

2.8 Histology and immunohistochemistry (IHC)

After imaging, the tongue and the mandibular lymph nodes with the salivary glands were fixed in 10% formalin (48 hours) while the lungs were fixed in Bouin's solution (12 hours). After fixation, the organs were embedded in paraffin blocks and sectioned for H&E staining to confirm the presence of the primary tumor and metastasis. In the orthotopic model, pan-cytokeratin (CK) staining (mouse monoclonal anti-human pan-CK antibody, 1:100, #M3515, Dako, CA, USA) of primary tumors, mandibular lymph nodes and lung metastases was also performed. Images were then acquired using a Nikon Eclipse 80i microscope (Nikon Inc., Melville, NY, USA). The brightness and contrast of the whole H&E and IHC images were further adjusted with ImageJ/Fiji (Schindelin et al., 2012).

2.9 Statistical analysis

Statistical analysis of quantification data was performed using one-way analysis of variance (ANOVA) followed by a post hoc Tukey test. Survival analysis was performed in both groups by the Kaplan-Meier method and the comparison between the two curves was performed by log-rank analysis using GraphPad Prism (GraphPad Software, San Diego, CA, USA).

3.Results

3.1 Growth of the primary tumor in the orthotopic model of OSCC

To develop the orthotopic tongue SCC model, we injected the novel HSC-3 cell line expressing GFP and luciferase into the tongues of athymic nude mice. HSC-3 cells were previously transduced with a GFP/Luc expression vector and further selected by FACS analysis for GFP expression (Figure S1). This cell line is then referred to as the HSC-3 GFP/Luc cell line. All 15 injected mice (5 male, 10 female) did not show any complications after tongue injection. Three female athymic nude mice were excluded from the study: two mice did not develop primary tumors and the third mouse was sacrificed 41 days after the injection due to otitis media with head tilt unrelated to the tumor growth.

Five female athymic nude mice were sacrificed between 32 and 44 days after injection due to weight loss and poor body condition score (BCS). Two male athymic nude mice with weight loss were sacrificed between 43 and 54 days after injection, while a third mouse died 60 days after injection due to tumor growth. The remaining two male mice were sacrificed 11 weeks after injection, while the remaining females were sacrificed 8 weeks after injection due to the higher morbidity. However, the difference between the two survival curves was not statistically significant by log-rank analysis (p=0.17) (Figure S2). The growth of the primary tumor as monitored over time by IVIS was different between the animals (Figure 1a,b). In two female mice, the orthotopic implantation was not successful. The quantification of the bioluminescence intensity by ROI analysis shows exponential growth of the signal until week 7.

3.2 The orthotopic model of OSCC presented lung and lymph node metastases by ex vivo imaging

The first bioluminescence signal from lung metastasis was detected 4 weeks after injection in one male mouse and increased until 60 days after injection (Figure 1c). At necropsy, multifocal metastatic yellow-whitish nodules in both lungs were observed (Figure 2a, L) and histopathological analysis of the regional lymph nodes showed the presence of metastases (Figure 2b-d). Histology of the primary tumor is also shown in Figure 2e-g. No evident bioluminescence signal from the lungs was observed in the other mice (n=11) prior to euthanasia (Figure 1c). In contrast, lymph node metastases were detected at necropsy (Figure 3a, black arrows) and by ex vivo imaging in 9 out of 11 mice (Figure 3b,c). Additionally, the ex vivo imaging of the lungs showed the presence of lung metastases in 5 more mice (3 male and 2 female mice, total distant metastasis rate=50%), which were sacrificed between 32 and 48 days after the injection. Quantification of the bioluminescence signal from the lung metastases is reported in Figure 3c. No liver metastases were detected. The mean signal from regional metastases ($2.50x10^7$) was more intense than the one from lung metastases ($1.35x10^6$). However, this difference was not statistically significant (p=0.85). The mean bioluminescence signal from the tongue tumor was $1.50x10^8$ photons/s and was significantly higher (p=0.007) than those from metastases (Figure 3c). Interestingly, the 5 mice

with lung metastasis also had lymph node metastasis. A separate ex vivo analysis of tumor and metastasis in male and female mice is reported in Figure S3.

3.3 Histology and pan-CK staining of the primary tumor and metastases

Mouse organs were processed for H&E and pan-CK staining to confirm the presence of the tongue tumor and the metastases detected by in vivo and/or ex vivo imaging. The results of the histopathological analysis were consistent with the bioluminescence signal. Representative images are shown in Figure 4. The tongue tumor presented an infiltrative growth into the muscular layer and had a high expression of pan-CK (Figure 4a). In regional lymph nodes, CK-positive tumor cells occurred in the subcapsular sinus and part of the cortex (Figure 4b, white arrows). Histology of the lungs showed a diffuse tumor cell infiltration (Figure 4c) or the presence of multifocal cellular aggregates indicating an early metastatic process (Figure 4d, white arrows).

3.4 Generation of HSC-3 M1 GFP/Luc cell line

To generate a novel cell line derived from HSC-3 lung metastases, we first injected HSC-3 GFP/Luc cells into the tail vein of 5 athymic nude mice. Two weeks after injection, large lung metastases developed in one athymic nude mouse and lungs were collected (Figure 5a-b). Metastatic tumor cells isolated from the lungs were then purified by FACS for GFP expression (Figure 5c). Stable luciferase expression of the sorted cells was observed by IVIS (Figure 5d**).** In contrast to HSC-3 cells, the newly isolated cells had an increased luciferase activity. The cells were then referred to as HSC-3 M1 GFP/Luc and expanded in vitro. Cell morphology is reported in Figure S4.

3.5 Non-orthotopic injection of HSC-3 M1 GFP/Luc cells produced large lung metastases

Three out of five HSC-3 M1 GFP/Luc-injected mice ($5x10^5$ cells injected; 60% metastasis rate) demonstrated metastases invading both lungs by in vivo and ex vivo imaging (Figure 6a-b). Histological confirmation of the lung metastases is reported in Figure 6c. Notably, IV injection of a lower number of HSC-3 GFP/Luc cells ($1x10^5$) also produced lung metastases in 3 out of 5 mice (60% metastasis rate; Figure S5). However, lung metastases invaded both lungs only in two cases (Figure S5).

4.Discussion

In OSCC, an increasing incidence of DMs and poor patient survival require further investigation of processes driving distant metastatic growth in vivo (Ishida et al., 2017; Steeg, 2016). In the present study, we established two mouse models of OSCC with a lung metastasis rate of 50-60% by using HSC-3 cells modified for GFP/Luc expression and HSC-3 M1 GFP/Luc cell line. In both models, histological analysis of the primary tumor and/or metastasis was consistent with the in vivo and ex vivo bioluminescence signal (Figures 1,3,4,6). The high rate of spontaneous lung metastases in our orthotopic model verified the accuracy of the orthotopic injection of tumor cells in mimicking the behaviour of several types of human cancers, including metastatic OSCC (Bais et al., 2015; Q. Li et al., 2020; Mognetti et al., 2006; Ohara et al., 2010; Saxena & Christofori, 2013; Tamada, Aoki, Nozawa, & Irimura, 2004).

Bais et al. (Bais et al., 2015) obtained a 100% lung metastasis rate only by orthotopic implantation of $0.5x10^6$ UMSCC2 cells, derived from a recurrent OSCC. Lung metastases were first observed by in vivo imaging 24 days after the injection and mandibular, liver, intestine, and bone metastases were also detected by day 31. However, only histology of the primary tumor was provided. Another study by Masood et al. (Masood et al., 2013) reported an orthotopic model of OSCC with lung metastases in 83% of the cases after 4 weeks using cells isolated from metastatic mice lymph nodes (USC-HN3-GFP-G1). Mermod et al. (Mermod et al., 2018) reported the development of lung metastasis only after the surgical removal of the primary tumor implanted in the submental area ($1x10^5$ cells, mEERL95 murine cell line). More recently, a syngeneic model reported by Chen et al. (Chen, Liu, et al., 2019) developed both lymph node and lung metastases 8 weeks after the orthotopic implantation of cells derived from 4NQO-induced OSCC (5×10^6 cells, MOC-L1-Luc murine cell subclone). However, the majority of developed orthotopic models of OSCC had no or very few lung metastases, probably due to the fast growth of the primary tumor and/or a high number of injected OSCC cells (e.g. $0.2\text{-}5x10^6$) accompanied by an early sacrifice of the animals (3-3.5 weeks) (Chen, Chang, Yang, Tu, & Lin, 2019; Matsui, Ota, Ueda, Tanino, & Odashima, 1998; Noguchi et al., 2003; Umeda et al., 2001).

Indeed, the orthotopic injection of $1.75x10^5$ HSC-3 cells and HSC-3 cells isolated from lymph node metastases (HSC-3 M3) in nude mice resulted in a low lung metastasis rate (10%) and a different lymph node metastasis rate (HSC-3:30%;HSC-3 M3:90%) evaluated by histology (Matsui et al., 1998). In contrast, we transduced HSC-3 cells using a lentivirus carrying both GFP and luciferase genes and used only $5x10^4$ HSC-3 GFP/Luc cells to establish our orthotopic model. In our model, lung metastases were first observed 4 weeks after implantation by in vivo imaging, while in the study by Matsui et al. (Matsui et al., 1998) the mice were sacrificed 3 weeks after injection. Moreover, the use of ex vivo bioluminescence imaging in our study allowed us to detect lung and lymph node metastases that were

not visible by in vivo imaging. The usefulness of this imaging technique to detect metastatic cells was also reported in other mouse models of OSCC (Bais et al., 2015; Braks et al., 2015; Chen, Chang, et al., 2019; Chen, Liu, et al., 2019; Masood et al., 2013). However, the bioluminescence imaging presents some limitations such as a transient and variable signal when compared to fluorescence imaging (Bais et al., 2015). In summary, our orthotopic model established with HSC-3 GFP/Luc cells presented advantages over the one established with solely HSC-3 cells (Matsui et al., 1998) such as the possibility of monitoring tumor growth in vivo and the presence of both lymph node (total regional metastasis rate=83%) and lung metastases (total distant metastasis rate=50%).

In addition, our study presented the development of lung metastasis without previous cell isolation from metastases and/or primary tumors (Q. Li et al., 2020; Masood et al., 2013) or surgical procedures (Mermod et al., 2018), consistent with the high metastatic potential in vivo of the HSC-3 cell line. Indeed, OSCC cell lines vary in origin and expression of important biomarkers such as human papillomavirus (HPV) proteins, TP53 mutations, and AP-1, which are involved in regional and distant metastatic progression (Hyakusoku et al., 2016; Mermod et al., 2018; Sano et al., 2011).

HPV-oropharyngeal SCC is characterised by frequent DMs and increasing incidence, and it is therefore separately classified from oral cavity SCC, which is usually not associated with HPV (Chi et al., 2015; Colevas et al., 2018; Furness et al., 2011; Irani, 2016a; Lu et al., 2018; Mermod et al., 2018). In oral cavity SCC, DMs have been reported especially in patients with tongue and gingiva SCC (Chi et al., 2015; Furness et al., 2011; Irani, 2016b; Osaki et al., 2000; Takahashi et al., 2014). In the study by Mermod et al. (Mermod et al., 2018), the mEERL cell line was generated by transforming mouse tonsillar epithelial cells with HPV16 E6-E7 proteins, while the human HSC-3 cell line derived from a highly metastatic tongue SCC and is a well-known HPV-negative cell line (Jouhi et al., 2015; Sugiyama et al., 2003).

The use of athymic nude mice lacking functional T lymphocytes in our orthotopic model hampers the evaluation of immunological processes involved in OSCC metastasis such as immune escape and immune modulation (Chen, Liu, et al., 2019; Q. Li et al., 2020; Mognetti et al., 2006). Immunocompromised mice are necessary when human cancer cell lines are used to reproduce tumors *in vivo* and different kinds have been used for xenograft models of OSCC (Q. Li et al., 2020; Rossa & D'silva, 2019). Interestingly, few orthotopic models of OSCC metastasis reported the use of severe immunocompromised mice such as SCID and NOD-SCID mice, which lack mature T and B lymphocytes and normal function of lymphocytes, NK cells, dendritic cells, and macrophages, respectively (Masood et al., 2013; Wu et al., 2017). Notably, athymic nude mice present the lowest degree of immune-

deficiency because of the presence of functional macrophages, dendritic cells, B lymphocytes, and neutrophils (Q. Li et al., 2020; Rossa & D'silva, 2019)

Of note, previous studies on HSC-3 cells showed a high expression of markers associated with OSCC recurrence and metastasis such as toll-like receptor (TLR) 5, metalloproteinases (MMPs) 2 and 3, and epithelial-to-mesenchymal transition (EMT) markers such as vimentin, N-cadherin, and MMP7 (Erdem, Carlson, Gerard, & Ichiki, 2007; Kauppila, Mattila, Karttunen, & Salo, 2013; W. Li, Zhu, & Qin, 2018). Indeed, a high expression of EMT markers such as vimentin, fibronectin, ZEB1, β-catenin, and/or MMP7, and a low E-cadherin expression were linked to the high regional and distant metastatic potential *in vivo* of newly established murine cell lines MOC-L1 and mEERL95 (Chen, Liu, et al., 2019; Mermod et al., 2018), and the human cell line USC-HN3-GFP-G2 (Masood et al., 2013). Moreover, cancer stem cells (CSCs) markers are emerging as important promoters of OSCC progression, recurrence, and metastasis (Masood et al., 2013; Wu et al., 2017). In an orthotopic model developed by Wu et al. (Wu et al., 2017), the lymph node metastasis rate obtained was 80% and 30% by using CD44+ and CD44- OSCC cells ($1x10^6$ cells, SCC9 cell line) respectively. However, the authors did not provide any information about the possible presence of lung metastasis. In contrast, other studies correlated the high level of aggressiveness and distant metastatic potential of OSCC cell lines with the expression of other CSCs markers such as OCT-4, ALDH1, and SOX2 and proliferation markers (Chen, Chang, et al., 2019; Chen, Liu, et al., 2019; Masood et al., 2013). Nevertheless, more investigations are needed in order to elucidate the role of EMT and CSCs in OSCC metastatic dissemination.

Furthermore, here we established an IV model by using for the first time OSCC cells isolated from a lung metastasis. Indeed, this procedure has previously been reported only for lymph node metastasis (Masood et al., 2013; Matsui et al., 1998). This allowed us to obtain large and diffuse lung metastases in 60% of the injected animals by week 3 by injecting a lower number of cells ($0.5x10^6$) than previous studies (Chen, Chang, et al., 2019; Hyakusoku et al., 2016; P. Li et al., 2012), indicating the high metastatic potential of HSC-3 M1 cell line. In addition, the prevalence and the distribution of lung metastases in both lungs were consistent with previous studies (Hyakusoku et al., 2016; P. Li et al., 2012; W. Li et al., 2018). A lung metastasis rate of 85 or 100% was obtained by injecting $1x10^6$ HSC-3 and $2x10^6$ CAL-27 cells, respectively, and in both models, coalescent metastatic nodules were observed in both lungs (Hyakusoku et al., 2016; P. Li et al., 2012) as in our IV model with HSC-3 M1 cells. However, our study has limitations such as the lack of HSC-3 M1 GFP/Luc cell line authentication and the use of the IV model. Indeed, this model (also referred to as "lung metastasis model") gives only lung metastasis and lacks the primary tumor and regional metastases, which are relevant for studying OSCC metastatic dissemination. Moreover, the number of injected cells is higher than those that may cause

lung metastasis in OSCC patients (Hyakusoku et al., 2016; Mognetti et al., 2006; Saxena & Christofori, 2013). Despite the IV model is still used to evaluate the distant metastatic potential of OSCC cells, including the newly isolated ones (Chen, Chang, et al., 2019; Chen, Liu, et al., 2019; Hyakusoku et al., 2016), we would suggest to rather use the orthotopic model to further investigate the development of OSCC DMs in vivo. Additionally, the IV model may mimic only the late stages of metastatic dissemination in a small subset of OSCC, since the presence of multiple metastases in both lungs was only reported in 8/35 patients with HNSCC lung metastasis (Osaki et al., 2000).

5.Conclusion

The poor prognosis for metastatic OSCC requires reliable preclinical models to study the early dissemination of metastatic cells in regional and distant organs and to evaluate novel therapies. The high rate of both lymph nodes and lung metastases, together with the presence of the primary tumor, makes our orthotopic model with HSC-3 GFP/Luc cells a promising tool for such purposes, when compared with the IV model. Although we demonstrated the high metastatic potential of the newly isolated HSC-3 M1 GFP/Luc cell line by IV injection, future studies using OSCC cell lines isolated from lung metastasis in orthotopic models may provide novel insights into OSCC metastatic progression.

Acknowledgments

MF gratefully acknowledges support from his Ernest Cockrell Jr. Presidential Distinguished Chair at Houston Methodist Research Institute. MF serves on the Board of Directors of Arrowhead Pharmaceuticals. Work by SM was partially supported by the Università Degli Studi di Milano. The authors thank Dr. Junhua Mai and Dr. Shen Qi, Department of Nanomedicine, Houston Methodist Research Institute for generously providing the lentivirus and assistance for the cellular transfection, David Haviland of the Flow Cytometry Core, Houston Methodist Research Institute for performing the cell sorting, and the Pathology Laboratory, Baylor College of Medicine for processing histology samples and performing pan-CK staining. We are also grateful to Prof. Eugenio Scanziani, Department of Veterinary Medicine, Università Degli Studi di Milano for help with histopathological analysis and to Dr. Stefan Siwko, Texas A&M Health Science Center for reviewing the manuscript.

Conflicts of interest:

None to declare.

Author Contributions

Conception and/or design of the study: SM, EB, EV, GL and MF. Data acquisition: SM, AD and GB. Data analysis and interpretation: SM, AD, GB, and EB. Manuscript writing and editing: SM, G.B, EB, EV, AD, GL, and MF. All authors reviewed the manuscript and gave their final approval.

References

Bais, M. V., Kukuruzinska, M., & Trackman, P. C. (2015). Orthotopic non-metastatic and metastatic oral cancer mouse models. *Oral Oncology*, *51*(5), 476–482. doi: 10.1016/j.oraloncology.2015.01.012

Bernier, J., Domenge, C., Ozsahin, M., Matuszewska, K., Lefèbvre, J.-L., Greiner, R. H., … European Organization for Research and Treatment of Cancer Trial 22931. (2004). Postoperative irradiation with or without concomitant chemotherapy for locally advanced head and neck cancer. *The New England Journal of Medicine*, *350*(19), 1945–1952. doi: 10.1056/NEJMoa032641

Braks, J. A. M., Spiegelberg, L., Koljenovic, S., Ridwan, Y., Keereweer, S., Kanaar, R., … Essers, J. (2015). Optical Imaging of Tumor Response to Hyperbaric Oxygen Treatment and Irradiation in an Orthotopic Mouse Model of Head and Neck Squamous Cell Carcinoma. *Molecular Imaging and Biology : MIB : The Official Publication of the Academy of Molecular Imaging*, *17*(5), 633–642. doi: 10.1007/s11307-015-0834-8

Chen, Y.-F., Chang, K.-W., Yang, I.-T., Tu, H.-F., & Lin, S.-C. (2019). Establishment of syngeneic murine model for oral cancer therapy. *Oral Oncology*, *95*, 194–201. doi: 10.1016/j.oraloncology.2019.06.026

Chen, Y.-F., Liu, C.-J., Lin, L.-H., Chou, C.-H., Yeh, L.-Y., Lin, S.-C., & Chang, K.-W. (2019). Establishing of mouse oral carcinoma cell lines derived from transgenic mice and their use as syngeneic tumorigenesis models. *BMC Cancer*, *19*(1), 281. doi: 10.1186/s12885-019-5486-7

Chi, A. C., Day, T. A., & Neville, B. W. (2015). Oral cavity and oropharyngeal squamous cell carcinoma--an update. *CA: A Cancer Journal for Clinicians*, *65*(5), 401–421. doi: 10.3322/caac.21293

Colevas, A. D., Yom, S. S., Pfister, D. G., Spencer, S., Adelstein, D., Adkins, D., … Darlow, S. D. (2018). NCCN Guidelines Insights: Head and Neck Cancers, Version 1.2018. *Journal of the National Comprehensive Cancer Network*, *16*(5), 479–490. doi: 10.6004/jnccn.2018.0026

de Visscher, S. A. H. J., Melchers, L. J., Dijkstra, P. U., Karakullukcu, B., Tan, I. B., Hopper, C., … Witjes, M. J. H. (2013). mTHPC-mediated Photodynamic Therapy of Early Stage Oral Squamous Cell Carcinoma: A Comparison to Surgical Treatment. *Annals of Surgical Oncology*, *20*(9), 3076–3082. doi: 10.1245/s10434-013-3006-6

Erdem, N. F., Carlson, E. R., Gerard, D. A., & Ichiki, A. T. (2007). Characterization of 3 Oral Squamous Cell Carcinoma Cell Lines With Different Invasion and/or Metastatic Potentials. *Journal of Oral and Maxillofacial Surgery*, *65*(9), 1725–1733. doi: 10.1016/j.joms.2006.11.034

Furness, S., Glenny, A.-M., Worthington, H. V, Pavitt, S., Oliver, R., Clarkson, J. E., … Conway, D. I. (2011). Interventions for the treatment of oral cavity and oropharyngeal cancer: chemotherapy. In S. Furness (Ed.), *Cochrane Database of Systematic Reviews* (p. CD006386). doi: 10.1002/14651858.CD006386.pub3

Harrington, K. J., Ferris, R. L., Blumenschein, G., Colevas, A. D., Fayette, J., Licitra, L., … Guigay, J. (2017). Nivolumab versus standard, single-agent therapy of investigator's choice in recurrent or metastatic squamous cell carcinoma of the head and neck (CheckMate 141): health-related quality-of-life results from a randomised, phase 3 trial. *The Lancet Oncology*, *18*(8), 1104–1115. doi: 10.1016/S1470-2045(17)30421-7

Hasegawa, T., Shibuya, Y., Takeda, D., Iwata, E., Saito, I., Kakei, Y., … Komori, T. (2017). Prognosis of oral squamous cell carcinoma patients with level IV/V metastasis: An observational study. *Journal of Cranio-Maxillo-Facial Surgery : Official Publication of the European Association for Cranio-Maxillo-Facial Surgery*, *45*(1), 145–149. doi: 10.1016/j.jcms.2016.10.011

Hier, M. P., Black, M. J., Shenouda, G., Sadeghi, N., & Karp, S. E. (1995). A murine model for the immunotherapy of head and neck squamous cell carcinoma. *The Laryngoscope*, *105*(10), 1077–1080. doi: 10.1288/00005537-199510000-00013

Hyakusoku, H., Sano, D., Takahashi, H., Hatano, T., Isono, Y., Shimada, S., … Oridate, N. (2016). JunB promotes cell invasion, migration and distant metastasis of head and neck squamous cell carcinoma. *Journal of Experimental & Clinical Cancer Research : CR*, *35*(1), 6. doi: 10.1186/s13046-016-0284-4

Irani, S. (2016a). Distant metastasis from oral cancer: A review and molecular biologic aspects. *Journal of International Society of Preventive & Community Dentistry*, *6*(4), 265–271. doi: 10.4103/2231-0762.186805

Irani, S. (2016b). Distant metastasis from oral cancer: A review and molecular biologic aspects. *Journal of International Society of Preventive and Community Dentistry*, *6*(4), 265. doi: 10.4103/2231-0762.186805

Ishida, K., Tomita, H., Nakashima, T., Hirata, A., Tanaka, T., Shibata, T., & Hara, A. (2017). Current mouse models of oral squamous cell carcinoma: Genetic and chemically induced models. *Oral Oncology*, *73*, 16–20. doi: 10.1016/j.oraloncology.2017.07.028

Jouhi, L., Datta, N., Renkonen, S., Atula, T., Mäkitie, A., Haglund, C., … Hagström, J. (2015). Expression of toll-like receptors in HPV-positive and HPV-negative oropharyngeal squamous cell carcinoma--an in vivo and in vitro study. *Tumour Biology : The Journal of the International Society for Oncodevelopmental Biology and Medicine*, *36*(10), 7755–7764. doi: 10.1007/s13277-015-3494-z

Kauppila, J. H., Mattila, A. E., Karttunen, T. J., & Salo, T. (2013). Toll-like receptor 5 (TLR5) expression is a novel predictive marker for recurrence and survival in squamous cell carcinoma of the tongue. *British Journal of Cancer*, *108*(3), 638–643. doi: 10.1038/bjc.2012.589

Kawashiri, S, Kumagai, S., Kojima, K., Harada, H., Nakagawa, K., & Yamamoto, E. (1999). Reproduction of occult metastasis of head and neck cancer in nude mice. *Clinical & Experimental Metastasis*, *17*(4), 277–282. Retrieved from http://www.ncbi.nlm.nih.gov/pubmed/10545013

Kawashiri, Shuichi, Noguchi, N., Tanaka, A., Nakaya, H., Kato, K., & Yamamoto, E. (2009). Inhibitory effect of neoadjuvant chemotherapy on metastasis of oral squamous cell carcinoma in a mouse model. *Oral Oncology*, *45*(9), 794–797. doi: 10.1016/j.oraloncology.2008.12.003

Li, P., Zhou, G., Zhu, X., Li, G., Yan, P., Shen, L., … Hamblin, M. R. (2012). Photodynamic therapy with hyperbranched poly(ether-ester) chlorin(e6) nanoparticles on human tongue carcinoma CAL-27 cells. *Photodiagnosis and Photodynamic Therapy*, *9*(1), 76–82. doi: 10.1016/j.pdpdt.2011.08.001

Li, Q., Dong, H., Yang, G., Song, Y., Mou, Y., & Ni, Y. (2020). Mouse Tumor-Bearing Models as Preclinical Study Platforms for Oral Squamous Cell Carcinoma. *Frontiers in Oncology*, *10*. doi: 10.3389/fonc.2020.00212

Li, W., Zhu, D., & Qin, S. (2018). SIRT7 suppresses the epithelial-to-mesenchymal transition in oral squamous cell carcinoma metastasis by promoting SMAD4 deacetylation. *Journal of Experimental & Clinical Cancer Research : CR*, *37*(1), 148. doi: 10.1186/s13046-018-0819-y

Lou, E., Kellman, R. M., Hutchison, R., & Shillitoe, E. J. (2003). Clinical and pathological features of the murine AT-84 orthotopic model of oral cancer. *Oral Diseases*, *9*(6), 305–312. Retrieved from http://www.ncbi.nlm.nih.gov/pubmed/14629332

Lu, D. J., Luu, M., Mita, A., Scher, K., Shiao, S. L., Yoshida, E. P., … Zumsteg, Z. S. (2018). Human papillomavirus-associated oropharyngeal cancer among patients aged 70 and older: Dramatically increased prevalence and clinical implications. *European Journal of Cancer (Oxford, England : 1990)*, *103*, 195–204. doi: 10.1016/j.ejca.2018.08.015

Masood, R., Hochstim, C., Cervenka, B., Zu, S., Baniwal, S. K., Patel, V., … Sinha, U. K. (2013). A novel orthotopic mouse model of head and neck cancer and lymph node metastasis. *Oncogenesis*, *2*(9), e68. doi: 10.1038/oncsis.2013.33

Matsui, T., Ota, T., Ueda, Y., Tanino, M., & Odashima, S. (1998). Isolation of a highly metastatic cell line to lymph node in human oral squamous cell carcinoma by orthotopic implantation in nude mice. *Oral Oncology*, *34*(4), 253–256. Retrieved from http://www.ncbi.nlm.nih.gov/pubmed/9813718

Mermod, M., Hiou-Feige, A., Bovay, E., Roh, V., Sponarova, J., Bongiovanni, M., … Simon, C. (2018). Mouse model of postsurgical primary tumor recurrence and regional lymph node metastasis progression in HPV-related head and neck cancer. *International Journal of Cancer*, *142*(12), 2518–2528. doi: 10.1002/ijc.31240

Mognetti, B., Di Carlo, F., & Berta, G. N. (2006). Animal models in oral cancer research. *Oral Oncology*, *42*(5), 448–460. doi: 10.1016/j.oraloncology.2005.07.014

Myers, J. N., Holsinger, F. C., Jasser, S. A., Bekele, B. N., & Fidler, I. J. (2002). An orthotopic nude mouse model of oral tongue squamous cell carcinoma. *Clinical Cancer Research : An Official Journal of the American Association for Cancer Research*, *8*(1), 293–298. Retrieved from http://www.ncbi.nlm.nih.gov/pubmed/11801572

Naruse, T., Yanamoto, S., Matsushita, Y., Sakamoto, Y., Morishita, K., Ohba, S., … Umeda, M. (2016). Cetuximab for the treatment of locally advanced and recurrent/metastatic oral cancer: An investigation of distant metastasis. *Molecular and Clinical Oncology*. doi: 10.3892/mco.2016.928

Noguchi, N., Kawashiri, S., Tanaka, A., Kato, K., & Nakaya, H. (2003). Effects of fibroblast growth inhibitor on proliferation and metastasis of oral squamous cell carcinoma. *Oral Oncology*, *39*(3), 240–247. Retrieved from http://www.ncbi.nlm.nih.gov/pubmed/12618196

Noguti, J., De Moura, C. F. G., De Jesus, G. P. P., Da Silva, V. H. P., Hossaka, T. A., Oshima, C. T. F., & Ribeiro, D. A. (n.d.). Metastasis from oral cancer: an overview. *Cancer Genomics & Proteomics*, *9*(5), 329–335. Retrieved from http://www.ncbi.nlm.nih.gov/pubmed/22990112

Ohara, T., Takaoka, M., Sakurama, K., Nagaishi, K., Takeda, H., Shirakawa, Y., … Naomoto, Y. (2010). The establishment of a new mouse model with orthotopic esophageal cancer showing the esophageal stricture. *Cancer Letters*, *293*(2), 207–212. doi: 10.1016/j.canlet.2010.01.017

Osaki, T., Yoneda, K., Yamamoto, T., Kimura, T., Matuoka, H., Sakai, H., & Ryoke, K. (2000). Clinical investigation on pulmonary metastasis of head and neck carcinomas. *Oncology*, *59*(3), 196–203. doi: 10.1159/000012161

Patel, V., Marsh, C. A., Dorsam, R. T., Mikelis, C. M., Masedunskas, A., Amornphimoltham, P., … Gutkind, J. S. (2011). Decreased Lymphangiogenesis and Lymph Node Metastasis by mTOR Inhibition in Head and Neck Cancer. *Cancer Research*, *71*(22), 7103–7112. doi: 10.1158/0008-5472.CAN-10-3192

Rossa, C., & D'silva, N. J. (2019). *Immune-relevant aspects of murine models of head and neck cancer*. doi: 10.1038/s41388-019-0686-9

Sano, D., & Myers, J. N. (2009). Xenograft models of head and neck cancers. *Head & Neck Oncology*, *1*(1), 32. doi: 10.1186/1758-3284-1-32

Sano, D., Xie, T.-X., Ow, T. J., Zhao, M., Pickering, C. R., Zhou, G., … Myers, J. N. (2011). Disruptive TP53 mutation is associated with aggressive disease characteristics in an orthotopic murine model of oral tongue cancer. *Clinical Cancer Research : An Official Journal of the American Association for Cancer Research*, *17*(21), 6658–6670. doi: 10.1158/1078-0432.CCR-11-0046

Saxena, M., & Christofori, G. (2013). Rebuilding cancer metastasis in the mouse. *Molecular Oncology*, *7*(2), 283–296. doi: 10.1016/j.molonc.2013.02.009

Schindelin, J., Arganda-Carreras, I., Frise, E., Kaynig, V., Longair, M., Pietzsch, T., … Cardona, A. (2012). Fiji: an open-source platform for biological-image analysis. *Nature Methods*, *9*(7), 676–682. doi: 10.1038/nmeth.2019

Steeg, P. S. (2016). Targeting metastasis. *Nature Reviews Cancer*, *16*(4), 201–218. doi: 10.1038/nrc.2016.25

Sugiura, T., Inoue, Y., Matsuki, R., Ishii, K., Takahashi, M., Abe, M., & Shirasuna, K. (2009). VEGF-C and VEGF-D expression is correlated with lymphatic vessel density and lymph node metastasis in oral squamous cell carcinoma: Implications for use as a prognostic marker. *International Journal of Oncology*, *34*(3), 673–680. Retrieved from http://www.ncbi.nlm.nih.gov/pubmed/19212672

Sugiyama, M., Bhawal, U. K., Dohmen, T., Ono, S., Miyauchi, M., & Ishikawa, T. (2003). Detection of human papillomavirus-16 and HPV-18 DNA in normal, dysplastic, and malignant oral epithelium. *Oral Surgery, Oral Medicine, Oral Pathology, Oral Radiology, and Endodontics*, *95*(5), 594–600. doi: 10.1067/moe.2003.36

Sutton, D. ., Brown, J. ., Rogers, S. ., Vaughan, E. ., & Woolgar, J. . (2003). The prognostic implications of the surgical margin in oral squamous cell carcinoma. *International Journal of Oral and Maxillofacial Surgery*, *32*(1), 30–34. doi: 10.1054/ijom.2002.0313

Takahashi, M., Aoki, T., Nakamura, N., Carreras, J., Kajiwara, H., Kumaki, N., … Ota, Y. (2014). Clinicopathological analysis of 502 patients with oral squamous cell carcinoma with special interest to

distant metastasis. *The Tokai Journal of Experimental and Clinical Medicine*, *39*(4), 178–185. Retrieved from http://www.ncbi.nlm.nih.gov/pubmed/25504205

Tamada, Y., Aoki, D., Nozawa, S., & Irimura, T. (2004). Model for paraaortic lymph node metastasis produced by orthotopic implantation of ovarian carcinoma cells in athymic nude mice. *European Journal of Cancer (Oxford, England : 1990)*, *40*(1), 158–163. Retrieved from http://www.ncbi.nlm.nih.gov/pubmed/14687800

Umeda, M., Yokoo, S., Komori, T., Nishimatsu, N., Shibuya, Y., & Fujioka, M. (2001). Experimental model of invasion and metastasis by orthotopic transplantation of oral squamous and adenoid cystic carcinomas into the tongue of nude mice. *The British Journal of Oral & Maxillofacial Surgery*, *39*(5), 376–380. doi: 10.1054/bjom.2000.0590

Wu, T.-F., Chen, L., Bu, L.-L., Gao, J., Zhang, W.-F., & Jia, J. (2017). CD44 + cancer cell-induced metastasis: A feasible neck metastasis model. *European Journal of Pharmaceutical Sciences*, *101*, 243–250. doi: 10.1016/j.ejps.2017.02.020

Xu, R., Zhang, G., Mai, J., Deng, X., Segura-Ibarra, V., Wu, S., … Shen, H. (2016). An injectable nanoparticle generator enhances delivery of cancer therapeutics. *Nature Biotechnology*, *34*(4), 414–418. doi: 10.1038/nbt.3506

Figure Captions

Figure 1 Results of the orthotopic model of oral cancer in athymic nude mice. *In vivo* imaging of representative HSC-3-injected male (**a**, left), female (**b**, left) mice and quantification of the bioluminescence signal of the primary tumor (**a,** right: week 1-5 n=5; week 6-7 n=4; week 8 n=3; week 9-10 n=2; **b,** right: week 1-4 n=7; week 5-6 n=3; week 7 n=2). In male mice, the highest tumor signal (10^9 photons/s) was detected in one mouse (arrow), which reached the endpoint between 7 and 8 weeks after the injection. The total emission (photons/s) was quantified per each bioluminescence region of interest (ROI). Data are expressed as the mean ± SEM. **c** *In vivo* imaging of HSC-3-injected male (left) and female mice (right): lung metastasis was detected only in one male mouse, which died 60 days after the injection.

Figure 2 Mouse with large lung metastases also developed lymph node metastases. a Lung metastases in one male athymic nude mouse (L, white arrows) and images of mandibular lymph nodes (metastasis indicated by the white arrow) with the salivary glands (LN) and tongue tumor (T). **b** and **c** Histology of mandibular lymph nodes, H&E staining, 100x magnification: tumor cells invaded the subcapsular sinus and part of the cortex (black arrows). **d** IHC staining, 100x magnification: metastatic cells expressed pan-cytokeratin (CK). Nonspecific plasma cells' CK staining (asterisk) was also present. **e** and **f** Histology of the primary tumor, H&E staining, 100x (**e**) and 400x magnification (**f**): the tongue carcinoma presented a high cellular density, with cells organised in islets and cordon-like structures and areas of keratinisation. At a higher magnification, the tumor cells had several features of malignancy such as pleomorphism, severe nuclear atypia, high nuclear/cytoplasmic ratio, and prominent nucleoli (black arrows). **g** IHC staining, 100x magnification**:** tumor cells presented a strong expression of pan-CK.

Figure 3 Ex vivo analysis of the primary tumor and metastasis in the orthotopic model of OSCC. a Representative images of mandibular lymph node metastases (black arrows) and primary tumors (black circles) at mice necropsy: the mandibular lymph nodes were collected with the salivary glands. **b** Representative e*x vivo* imaging in one mouse to detect the presence of tumor cells in the tongue and the other organs/tissues. Large tumor metastases were observed in regional lymph nodes**.** T= tongue, LN= regional lymph nodes and salivary glands, LV= liver, S= spleen, L=lungs. **c** Quantification of bioluminescence data for *ex vivo* analysis of the primary tumor and metastases in both sexes of athymic nude mice. Photons/s emitted by the primary tumor (n=11), the regional lymph nodes (n=9), and the lung metastases (n=5) were quantified and expressed as the mean ± SEM. Representative images of the primary tumor and metastasis are shown (right panel). ** $p < 0.01$ by one-way ANOVA with *post hoc* Tukey test.

Figure 4 Histology of the primary tumor and metastases in the orthotopic model. Representative images of H&E (top) and pan-CK staining (bottom) of the primary tumor (**a**), lymph node (**b**), and lung metastases (**c-d**). **a** Histological analysis of the primary tumor revealed the presence of areas of keratinisation. Cellular architecture consisted of cordon-like structures and cellular islets. DEp= dorsal epithelium; VEp= ventral epithelium. **b** In the mandibular lymph nodes, CK was expressed on the membrane of the metastatic cells**.** Nonspecific plasma cells' CK staining (asterisk) and CK-negative histiocytic areas (black arrows) were also present. **c** Histology of the lungs reported in Figure 2a: a diffuse tumor cell infiltration in both lungs and strong pan-CK staining were observed. **d** Histology of the lung metastases previously detected by *ex vivo* imaging: representative images of H&E and pan-CK staining. Several cellular aggregates (white arrows) were observed. Nonspecific staining of plasma in blood vessels was also present.

Figure 5 Isolation of HSC-3 M1 cell line. a *In vivo* imaging of the HSC-3-injected athymic nude mouse from which HSC-3 M1 cells were isolated. **b** Representative images of lung metastases at necropsy. Both lungs presented with metastatic nodules (circles). **c** FACS of the isolated cells for GFP expression: almost 20% of the analysed cells was strongly positive for GFP. The GFP signal detected in the sorted population was between 10^4 and 10^5 (lower panel on the right). **d** *In vitro* bioluminescence imaging on sorted HSC-3 M1 GFP/Luc cells (left). Less linear dependence than HSC-3 cells was observed (right). The cells were serially diluted 1:2 from 500,000 to 7800 in a 96-well plate. DMEM media served as a negative control (IVIS Spectrum Perkin Elmer Inc., Waltham, MA).

Figure 6 HSC-3 M1 induced metastases upon IV injection in athymic nude mice. a *In vivo* imaging of HSC-3 M1-injected athymic nude female mice. Five weeks after the IV injection of tumor cells, large lung metastases were detected in 60% of the mice. **b** *Ex vivo* imaging of mouse organs was performed 6 weeks after the injection to detect the presence of tumor cells. No liver metastases were detected. L=lungs; LV=liver; S=spleen. **c** H&E staining of the lung metastases in the IV model with HSC-3 M1 cell line. Metastases initially detected by *in vivo* imaging were further confirmed by histology. Representative images of OSCC lung metastasis show a diffuse tumor cell infiltration (arrows) in both lungs. At a higher magnification (400x), pleomorphism, anisocytosis, marked nuclear atypia, and prominent nucleolus characterised the HSC-3 M1 cells.

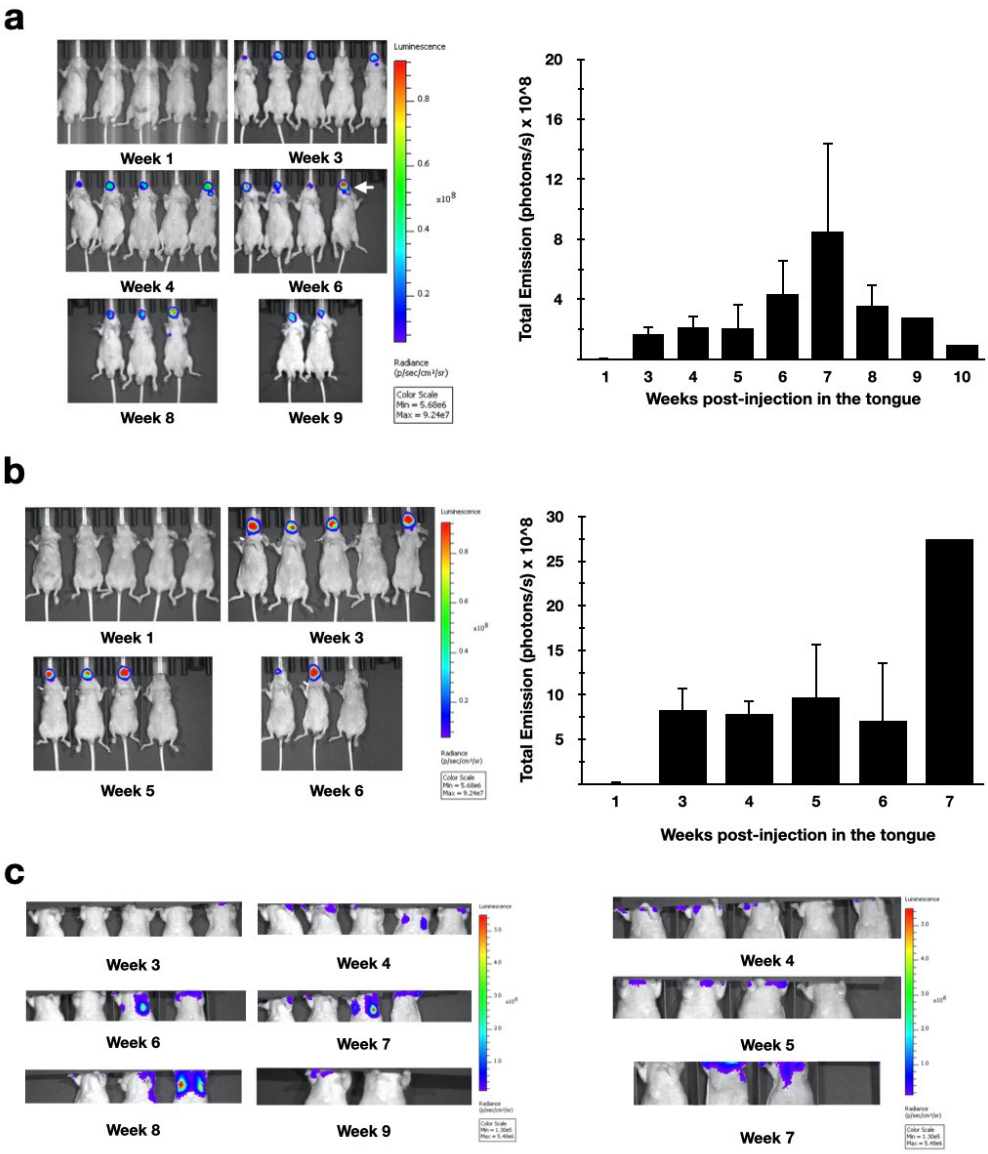

Figure 1 Results of the orthotopic model of oral cancer in athymic nude mice. In vivo imaging of representative HSC-3-injected male (a, left), female (b, left) mice and quantification of the bioluminescence signal of the primary tumor (a, right: week 1-5 n=5; week 6-7 n=4; week 8 n=3; week 9-10 n=2; b, right: week 1-4 n=7; week 5-6 n=3; week 7 n=2). In male mice, the highest tumor signal (10^9 photons/s) was detected in one mouse (arrow), which reached the endpoint between 7 and 8 weeks after the injection. The total emission (photons/s) was quantified per each bioluminescence region of interest (ROI). Data are expressed as the mean ± SEM. c In vivo imaging of HSC-3-injected male (left) and female mice (right): lung metastasis was detected only in one male mouse, which died 60 days after the injection.

86x101mm (300 x 300 DPI)

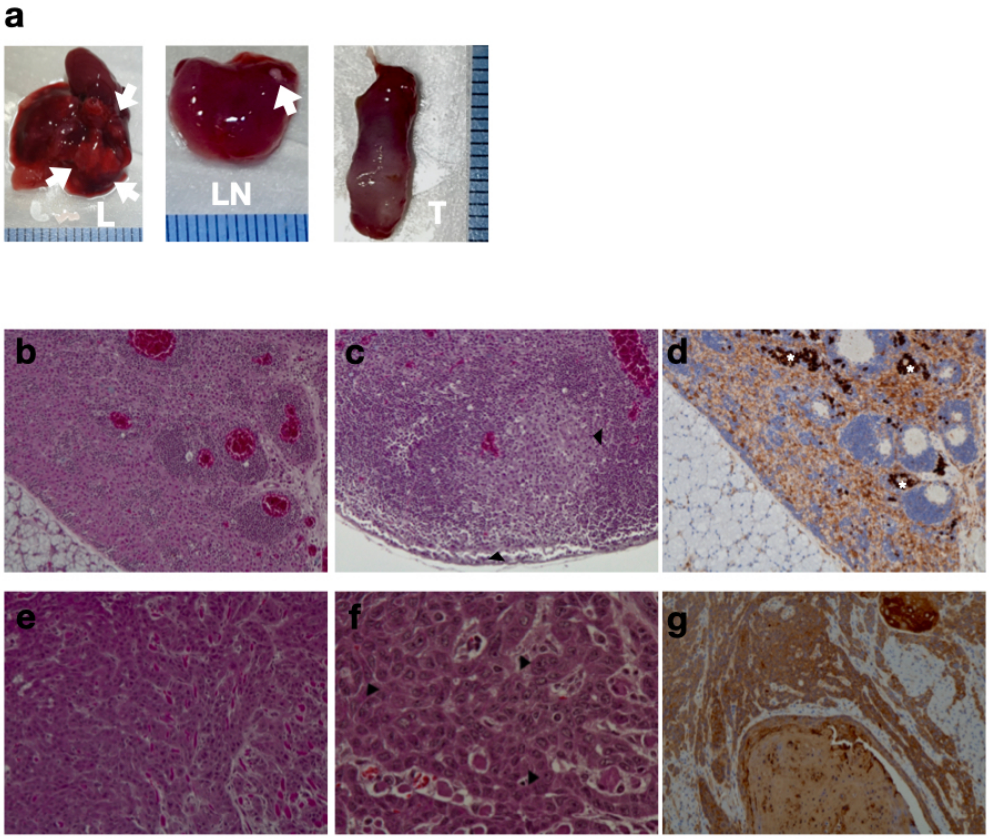

Figure 2 Mouse with large lung metastases also developed lymph node metastases. a Lung metastases in one male athymic nude mouse (L, white arrows) and images of mandibular lymph nodes (metastasis indicated by the white arrow) with the salivary glands (LN) and tongue tumor (T). b and c Histology of mandibular lymph nodes, H&E staining, 100x magnification: tumor cells invaded the subcapsular sinus and part of the cortex (black arrows). d IHC staining, 100x magnification: metastatic cells expressed pan-cytokeratin (CK). Nonspecific plasma cells' CK staining (asterisk) was also present. e and f Histology of the primary tumor, H&E staining, 100x (e) and 400x magnification (f): the tongue carcinoma presented a high cellular density, with cells organised in islets and cordon-like structures and areas of keratinisation. At a higher magnification, the tumor cells had several features of malignancy such as pleomorphism, severe nuclear atypia, high nuclear/cytoplasmic ratio, and prominent nucleoli (black arrows). g IHC staining, 100x magnification: tumor cells presented a strong expression of pan-CK.

76x67mm (300 x 300 DPI)

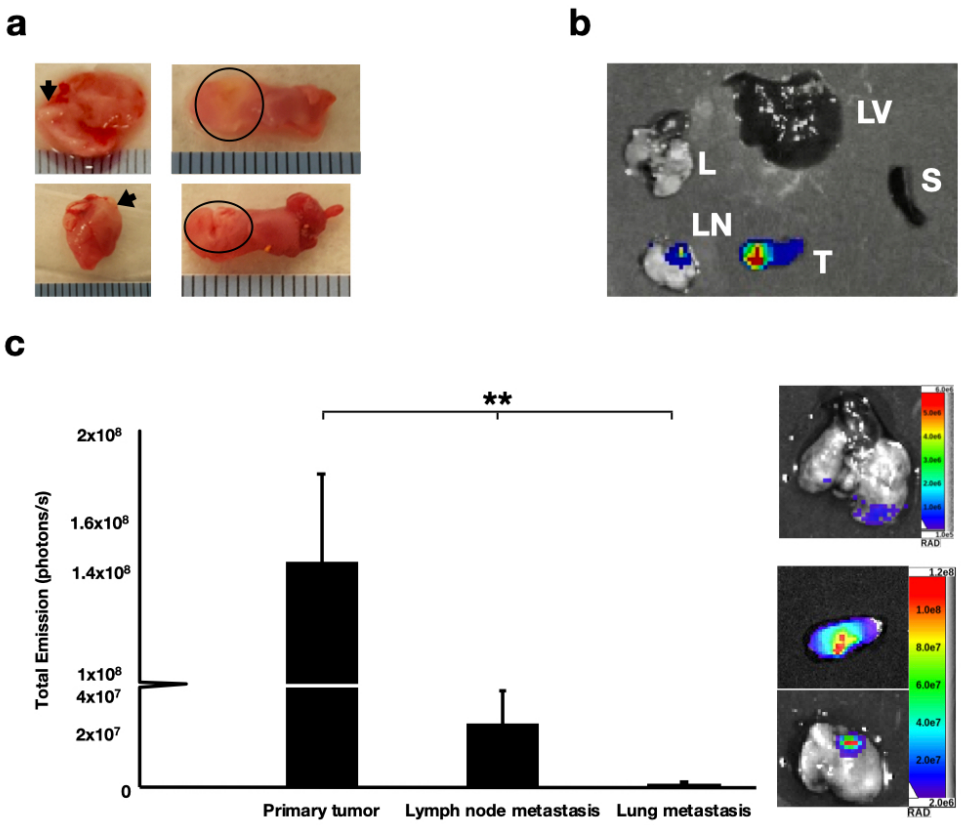

Figure 3 Ex vivo analysis of the primary tumor and metastasis in the orthotopic model of OSCC. a Representative images of mandibular lymph node metastases (black arrows) and primary tumors (black circles) at mice necropsy: the mandibular lymph nodes were collected with the salivary glands. b Representative ex vivo imaging in one mouse to detect the presence of tumor cells in the tongue and the other organs/tissues. Large tumor metastases were observed in regional lymph nodes. T= tongue, LN= regional lymph nodes and salivary glands, LV= liver, S= spleen, L=lungs. c Quantification of bioluminescence data for ex vivo analysis of the primary tumor and metastases in both sexes of athymic nude mice. Photons/s emitted by the primary tumor (n=11), the regional lymph nodes (n=9), and the lung metastases (n=5) were quantified and expressed as the mean ± SEM. Representative images of the primary tumor and metastasis are shown (right panel). ** $p < 0.01$ by one-way ANOVA with post hoc Tukey test.

86x76mm (300 x 300 DPI)

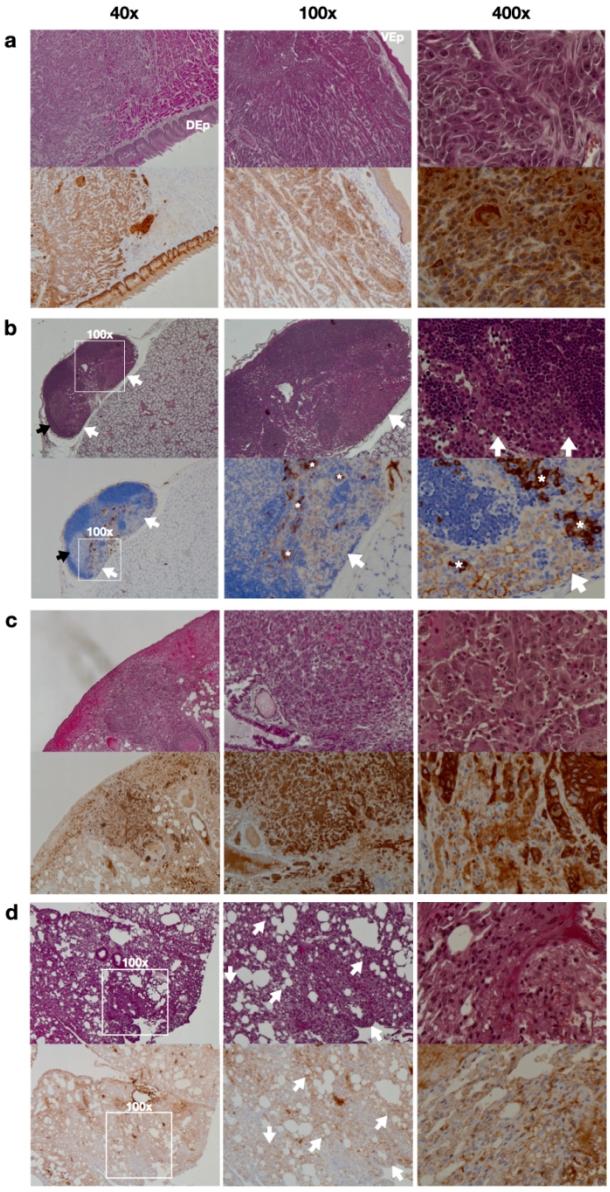

Figure 4 Histology of the primary tumor and metastases in the orthotopic model. Representative images of H&E (top) and pan-CK staining (bottom) of the primary tumor (a), lymph node (b), and lung metastases (c-d). a Histological analysis of the primary tumor revealed the presence of areas of keratinisation. Cellular architecture consisted of cordon-like structures and cellular islets. DEp= dorsal epithelium; VEp= ventral epithelium. b In the mandibular lymph nodes, CK was expressed on the membrane of the metastatic cells. Nonspecific plasma cells' CK staining (asterisk) and CK-negative histiocytic areas (black arrows) were also present. c Histology of the lungs reported in Figure 2a: a diffuse tumor cell infiltration in both lungs and strong pan-CK staining were observed. d Histology of the lung metastases previously detected by ex vivo imaging: representative images of H&E and pan-CK staining. Several cellular aggregates (white arrows) were observed. Nonspecific staining of plasma in blood vessels was also present.

86x152mm (300 x 300 DPI)

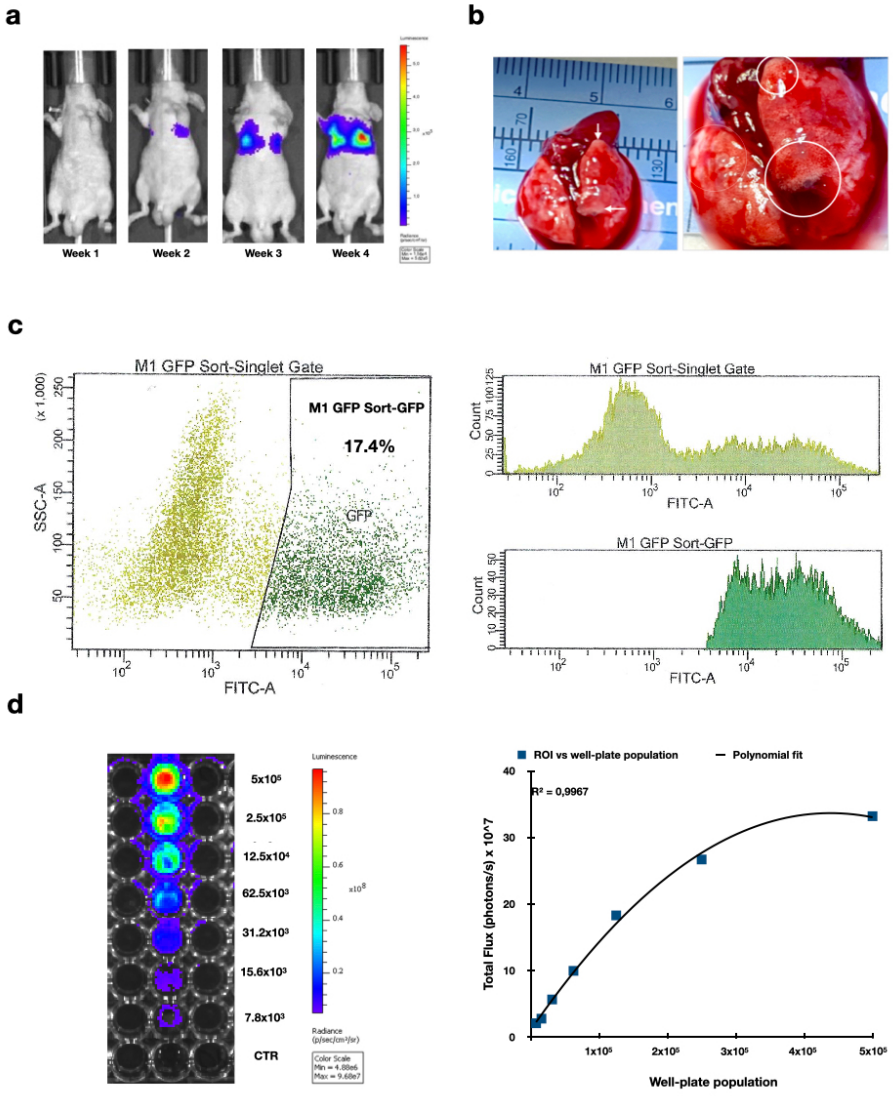

Figure 5 Isolation of HSC-3 M1 cell line. a In vivo imaging of the HSC-3-injected athymic nude mouse from which HSC-3 M1 cells were isolated. b Representative images of lung metastases at necropsy. Both lungs presented with metastatic nodules (circles). c FACS of the isolated cells for GFP expression: almost 20% of the analysed cells was strongly positive for GFP. The GFP signal detected in the sorted population was between 10^4 and 10^5 (lower panel on the right). d In vitro bioluminescence imaging on sorted HSC-3 M1 GFP/Luc cells (left). Less linear dependence than HSC-3 cells was observed (right). The cells were serially diluted 1:2 from 500,000 to 7800 in a 96-well plate. DMEM media served as a negative control (IVIS Spectrum Perkin Elmer Inc., Waltham, MA).

86x101mm (300 x 300 DPI)

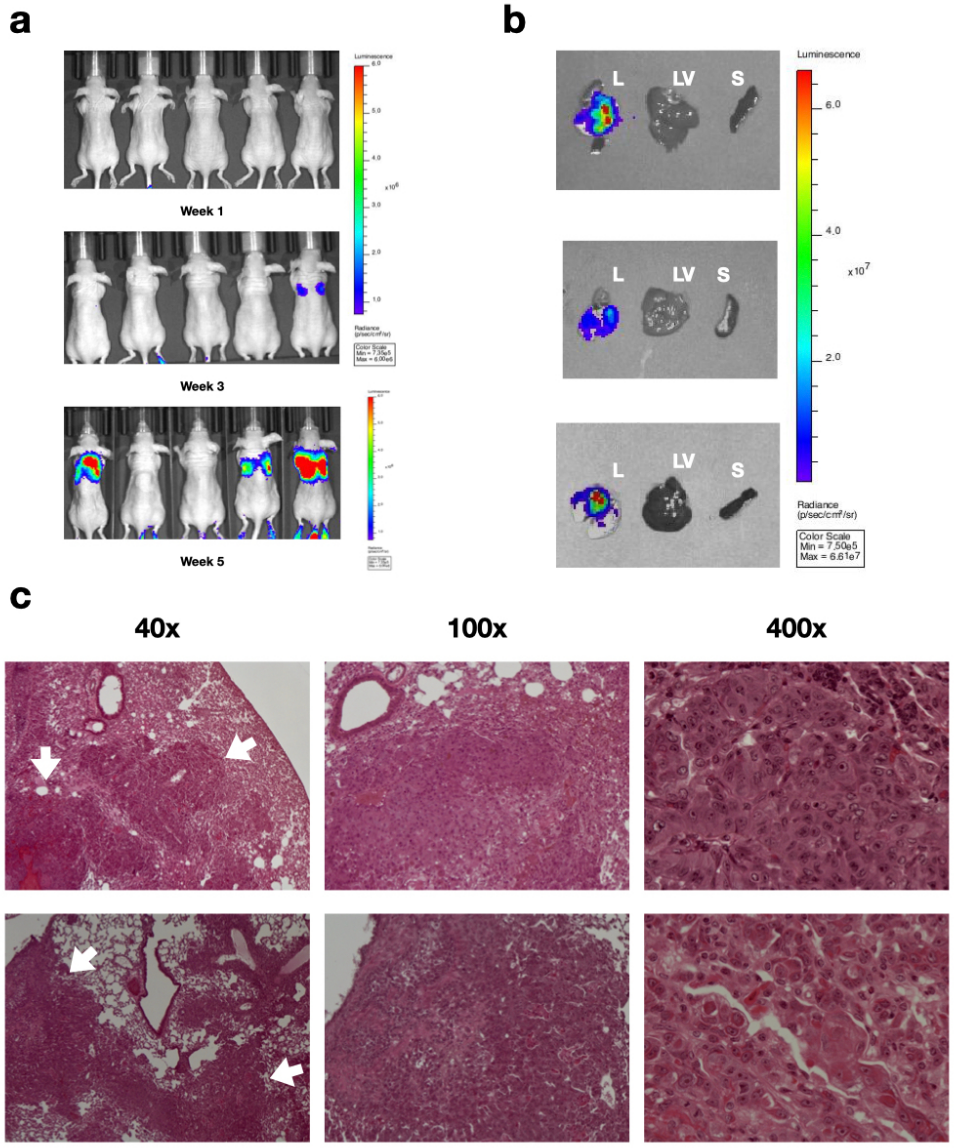

Figure 6 HSC-3 M1 induced metastases upon IV injection in athymic nude mice. a In vivo imaging of HSC-3 M1-injected athymic nude female mice. Five weeks after the IV injection of tumor cells, large lung metastases were detected in 60% of the mice. b Ex vivo imaging of mouse organs was performed 6 weeks after the injection to detect the presence of tumor cells. No liver metastases were detected. L=lungs; LV=liver; S=spleen. c H&E staining of the lung metastases in the IV model with HSC-3 M1 cell line. Metastases initially detected by in vivo imaging were further confirmed by histology. Representative images of OSCC lung metastasis show a diffuse tumor cell infiltration (arrows) in both lungs. At a higher magnification (400x), pleomorphism, anisocytosis, marked nuclear atypia, and prominent nucleolus characterised the HSC-3 M1 cells.

86x101mm (300 x 300 DPI)

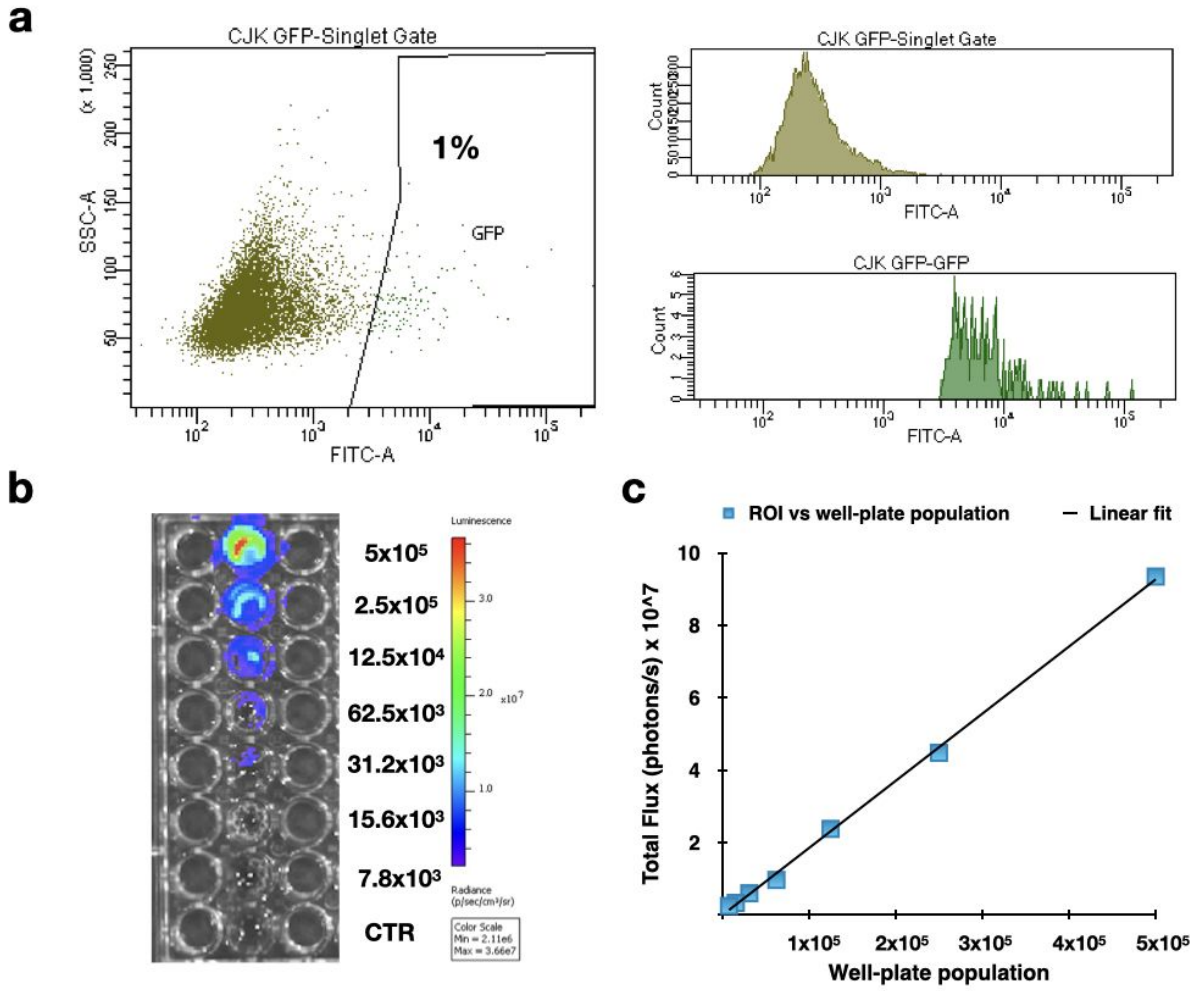

Figure S1 GFP/luciferase expression of transduced HSC-3 cells. a Transduced HSC-3 cells were selected by Fluorescence-activated cell sorting (FACS) for GFP expression: results showed 1% of transduced cells positive for GFP (BD FACSAria II Cell Sorter). **b** *In vitro* bioluminescence imaging on sorted GFP/Luc-transduced HSC-3 cells. The cells were serially diluted 1:2 from 500,000 to 7800 in a 96-well plate and were imaged after the addition of luciferin to the media (IVIS Spectrum Perkin Elmer Inc., Waltham, MA). DMEM media served as a negative control. **c** The quantification plot shows the linear fit between the serial dilutions and signal intensity using the bioluminescence region of interest (ROI) (R^2 = 0.99).

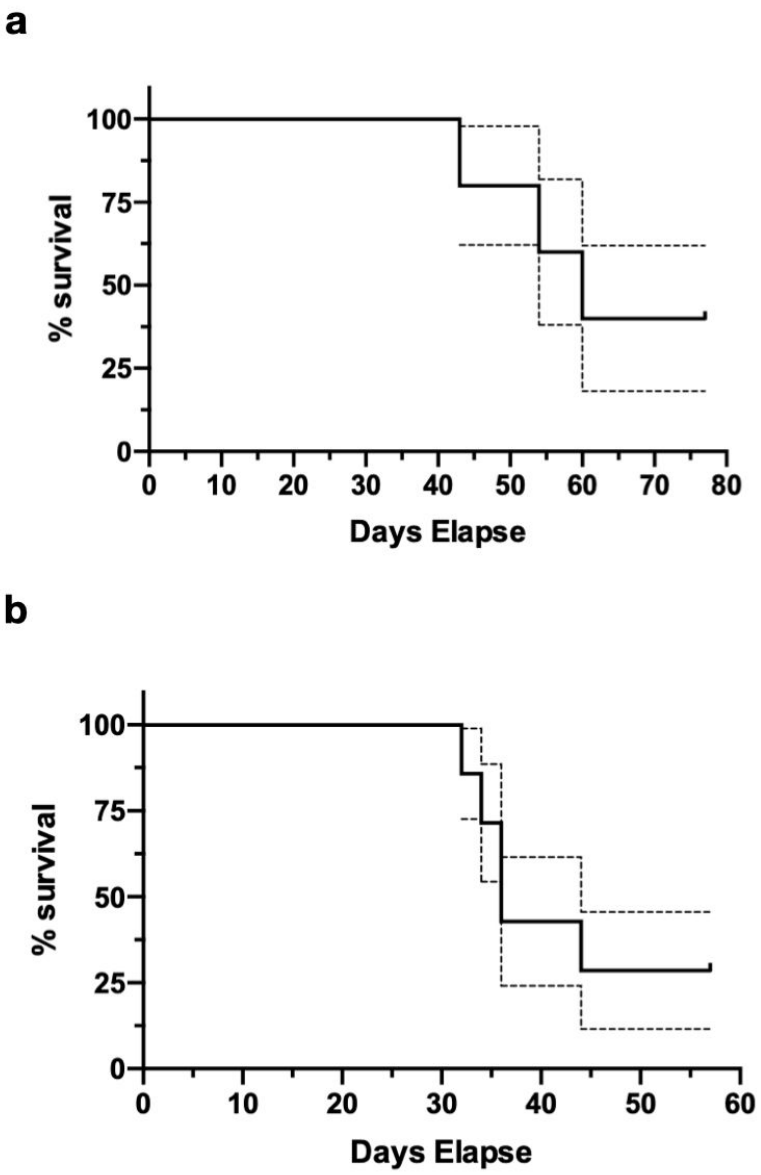

Figure S2 Survival of athymic nude mice with OSCC. Survival curve of male (**a**, n=5) and female (**b**, n=7) athymic nude mice. The median survival of male and female mice was 60 and 36 days respectively. Error bars are plotted as SE.

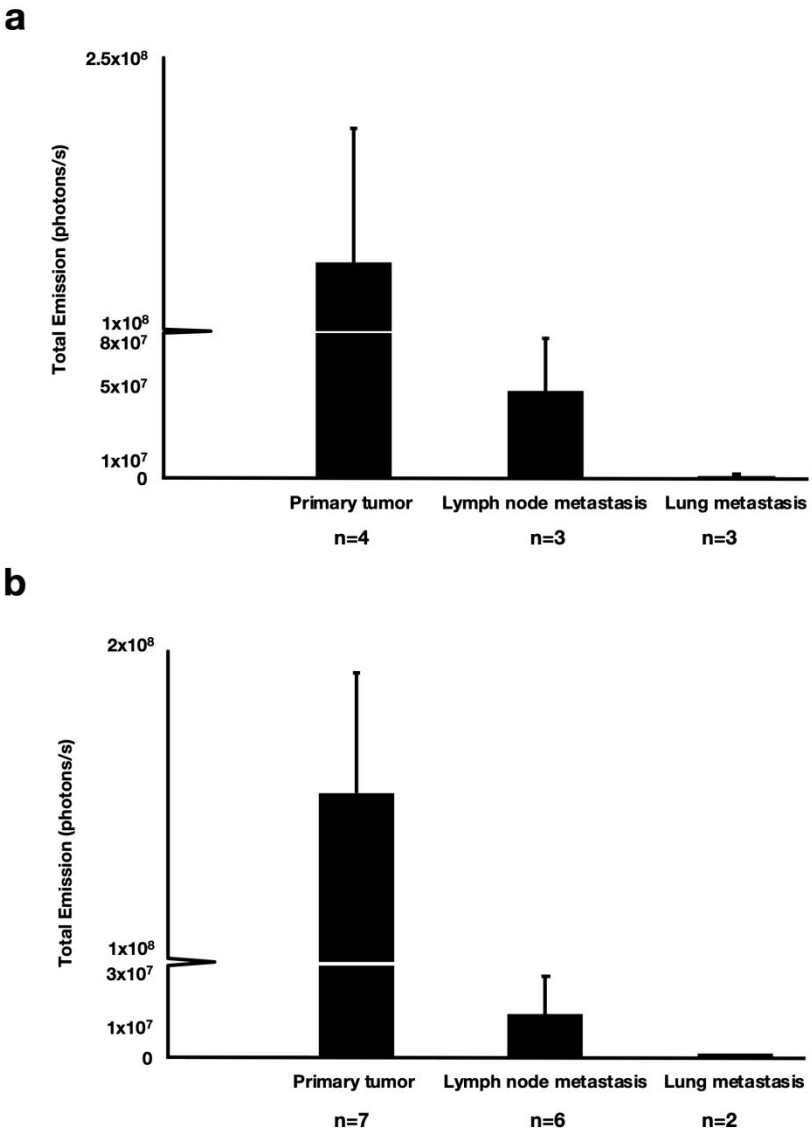

Figure S3 Quantification of bioluminescence signal of the primary tumor and metastases in male and female athymic nude mice. Photons/s emitted by the tongue, the lymph nodes, and lung metastases were quantified and are shown as mean ± SEM. **a** and **b** represent the *ex vivo* analysis of tumor and metastases in male and female mice respectively. While the mean signal of the primary tumor was similar between the two graphs ($1.38x10^8$ vs $1.55x10^8$), the signal of lymph node metastases in male mice was three times higher than in female mice ($4.82x10^7$ vs $1.39x10^7$).

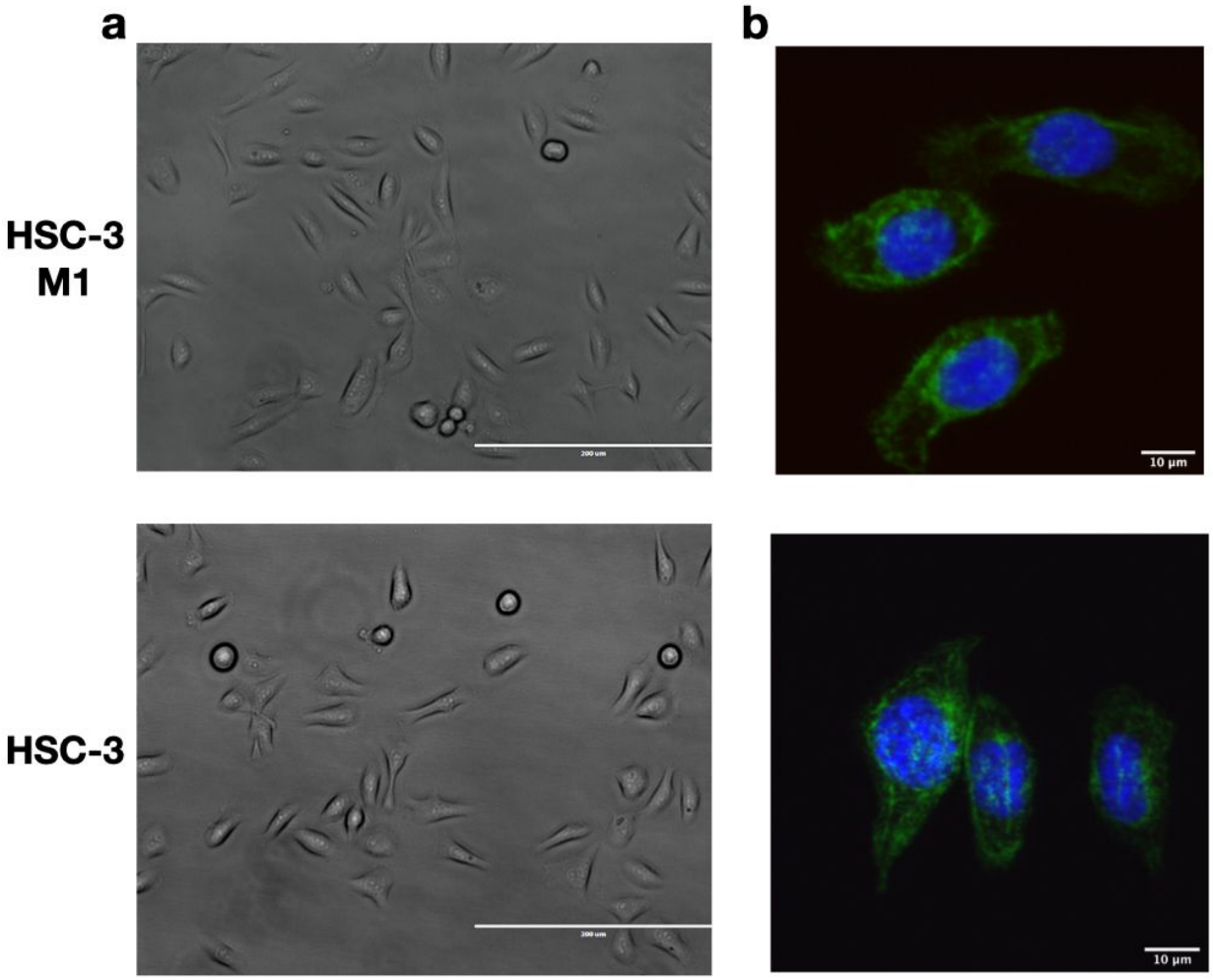

Figure S4 Morphology of HSC-3 M1 GFP/Luc and HSC-3 cells by light and confocal microscopy. a The new HSC-3 M1 cell line conserved the round to spindle morphology of the parental HSC-3 cells when observed under light microscopy (20x, EVOS FLTM, American Microscope Group). The spindle-shaped morphology of HSC-3 and HSC-3 M1 cells is consistent with epithelial-to-mesenchymal transition (EMT). Scale bar represents 200 µm. **b** Representative zeta stack projections of HSC-3 M1 GFP/Luc and HSC-3 cells (ImageJ). Alexa Fluor 488 phalloidin (green fluorescence) and DAPI (blue fluorescence) were used to stain the cytoskeleton and the nucleus, respectively. Scale bar represents 10 µm.

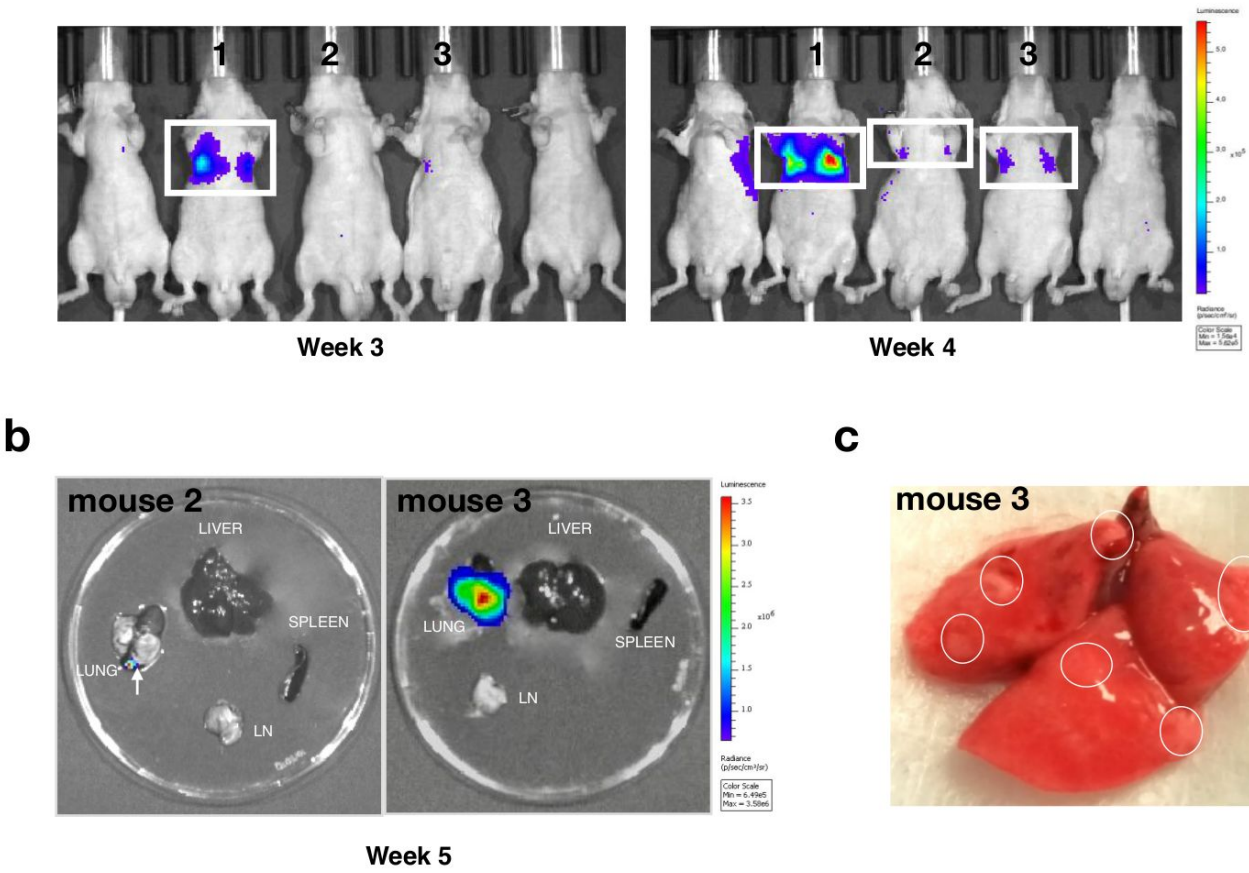

Figure S5 Injection of HSC-3 GFP/Luc cells in athymic nude mice. a *In vivo* imaging of all 5 HSC-3-injected athymic nude mice. The novel HSC-3 M1 cell line was isolated from mouse "1" (see also Figure 5). Four weeks after the injection, smaller lung metastases were detected in 2 other mice (mouse "2" and mouse "3"). **b** *Ex vivo* imaging was performed 5 weeks after the injection to confirm the metastases detected by *in vivo* imaging. While mouse "3" presented diffuse lung metastases in both lungs, mouse "2" presented a small lung metastasis only in one lung. No lung metastases were detected *ex vivo* in the other two mice. LN= mandibular lymph nodes with salivary glands. **c** Representative macroscopic image of lung metastases in mouse "3". The lung metastases were macroscopically observed (circles), although they were not as large and evident as the ones in mouse "1" (Figure 5b).